

FLOATING DOPPLER WIND LIDAR MOTION SIMULATOR FOR HORIZONTAL WIND SPEED MEASUREMENT ERROR ASSESSMENT

*Salcedo-Bosch, A.¹, Farré-Guarné J.¹, Sala-Álvarez, J.² Senior member, IEEE, Villares-Piera J.²,
Tanamachi, R.L.³, Rocadenbosch, F.^{1,4} Senior member, IEEE*

¹CommSensLab-UPC, Department of Signal Theory and Communications (TSC), Universitat Politècnica de Catalunya (UPC)

²Department of Signal Theory and Communications (TSC), UPC

³Department of Earth, Atmospheric, and Planetary Sciences (EAPS), Purdue University, West Lafayette, IN 47907 USA,

⁴Institut d'Estudis Espacials de Catalunya (Institute of Space Studies of Catalonia, IEEC), Barcelona, Spain, E-08034 Barcelona, Spain

Correspondence: andreu.salcedo@upc.edu (A. S.-B.); roca@tsc.upc.edu (F.R.)

ABSTRACT

This study presents a wind retrieval simulator of a floating Doppler Wind Lidar (DWL) with 6 Degrees of Freedom (DoF) motion. The simulator considers a continuous-wave conical-scanning floating DWL which retrieves the wind vector from 50

This work was supported via Spanish Government–European Regional Development Funds project PGC2018-094132-B-I00 and H2020 ACTRIS-IMP (GA-871115). The European Institute of Innovation and Technology (EIT), KIC InnoEnergy project NEPTUNE (Offshore Metocean Data Measuring Equipment and Wind, Wave and Current Analysis and Forecasting Software, call FP7) supported measurements campaigns. CommSensLab is a María-de-Maeztu Unit of Excellence funded by the Agencia Estatal de Investigación (Spanish National Science Foundation). The work of Andreu Salcedo was supported by the “Agència de Gestió d’Ajuts Universitaris i de la Recerca (AGAUR)”, Generalitat de Catalunya, under Grant no. 2020 FISDU 00455.

7 radial velocities per scan. The 6 DoF motion framework as well as the most important buoy motion equations are summarized.
8 Rotational and translational motion effects over HWS measurements are studied parametrically.

9 ***Index Terms***— DWL, floating, 6 DoF, simulator, VAD, error, wind.

10 1. INTRODUCTION

11 In the offshore wind-energy context Floating Doppler Wind Lidars (FDWL) are one of the most suitable candidates to replace
12 metmasts. When placed over floating platforms or buoys, DWLs can assess the wind resource in a cost-effective way [1].
13 Moreover, they can be easily re-deployed at multiple locations being able to cover large areas offering high versatility. However,
14 one of the main FDWL shortcomings is the wave-induced motion influence on wind measurements.

15 Sea waves induce translational (surge, sway and heave for x, y and z axes, respectively) and rotational (roll, pitch, and yaw
16 for x, y and z axes, respectively) motion, which add up to 6 degrees of freedom (DoF). On one hand, translational and rotational
17 velocities create an apparent Doppler effect on the retrieved wind vector and turbulence intensity (TI) measurements. On the
18 other hand, the buoy's tilt impacts the lidar pointing direction at each line of Sight (LoS) of the DWL scanning pattern [2]. In the
19 wind energy time basis (10 min) DWL measurement errors on mean wind vector are averaged out. However, TI measurements,
20 related to HWS standard deviation, suffer a noticeable impact. In [3], a complete description of the lidar attitude is given. The
21 DWL retrieves the wind vector from the LoSs by means of the velocity azimuth display (VAD) algorithm. The complexity of
22 vector transformations and high non-linearity of the VAD algorithm suggest the development of a FDWL simulator. A basic
23 FDWL simulator was presented in [4]. It has been used in FDWL motion compensation studies [5]. In this work, we present an
24 updated simulator by adding the 6 DoF motion equations to study the effect of 6 DoF motion on the DWL-retrieved HWS.

25 This paper is structured as follows: section 2 describes the geometry of the motional problem along with the FDWL
26 simulator; section 3 analyses the motion influence on the retrieved HWS and finally; section 4 gives concluding remarks.

2. METHODS

Here we consider the scenario of a ZephIR300 FDWL vertically aimed. It measures 50 radial velocities in a conical scan pattern by deflecting the lidar focus by means of a rotating prism. The 50 LoSs are sampled at a frequency of 1 scan/s at a cone width of 30.6 deg. The VAD algorithm retrieves the wind vector components (u, v, w) from the wind vector projections on each of the LoS along the conical scan pattern by fitting a sinusoidal wave to the measured LoSs [6]. Here we follow a similar approach to that nicely presented in [3]. A geometrical scheme of the FDWL buoy system is depicted in Fig. 1. In the absence of external rotational or translational forces, the X, Y, and Z axes of the buoy's moving body Cartesian right-handed XYZ coordinate system are aligned with the North-East-Down fixed Cartesian right-handed NED coordinate system. In real operating conditions external forces induce translational (sway, surge and heave) and rotational (roll, pitch and yaw) motion along the N, E and D directions. We define \hat{n} , \hat{e} , and \hat{d} as unitary vectors aligned with the NED axes of the fixed coordinate

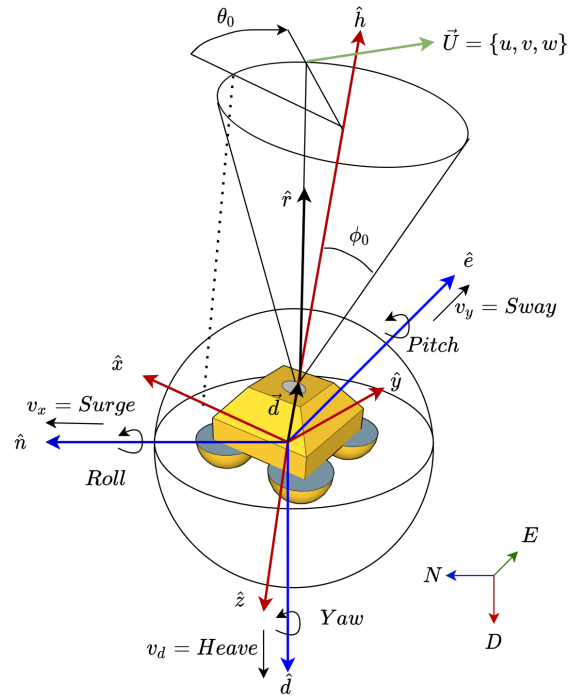


Fig. 1. Schematic of the geometry of the floating lidar representing the scanning cone and the fixed (blue arrows) and moving (red arrows) coordinate systems. Adapted from [3].

37 system. On the other hand, \hat{x} , \hat{y} , and \hat{z} are defined as unitary vectors aligned with the XYZ moving-body coordinate system and
 38 \hat{h} is defined as the unit vector opposite to \hat{z} . Moreover, we define \vec{d} as the separation vector between NED origin and the lidar
 39 prism. The LoSs measured by the lidar are scanned in a cone of ϕ_0 width from \hat{h} . We define θ_0 as the lidar initial scan phase,
 40 i.e., the azimuth angle between the first LoS of the scanning pattern and unitary vector \hat{x} . During a conical scan, moving vector
 41 \hat{r} varies from $\phi = \phi_0$ deg to $\phi = \phi_0 + 360$ deg. Multiple vector rotations are applied to transform the rotational motion, i.e.,
 42 roll, pitch, and yaw angles, into the real lidar pointing direction \hat{r} in the NED coordinate system.

43 The LoS velocities measured by the DWL are influenced by the buoy's rotational and translational velocities at the lidar
 44 prism. The velocity vector at the lidar prism is defined as

$$v_{\vec{lidar}} = \hat{n}v_x + \hat{e}v_y + \hat{d}v_d + (\hat{n}\omega_x) \times \vec{d} + (\hat{e}\omega_y) \times \vec{d}, \quad (1)$$

45 where v_x , v_y and v_d are surge, sway and heave velocities, and ω_x and ω_y are roll and pitch rotational velocities, respectively.

46 The lidar velocity influence to the LoSs is determined by

$$v_{LoS} = \hat{r} \cdot v_{\vec{lidar}}. \quad (2)$$

47 *6-DoF motion simulation and dimension reduction.*- A motion simulation with the fundamental motional equations of a FDWL
 48 presented in [3] has been implemented. A time-static and spatially-uniform wind field \vec{U} in the absence of turbulence is
 49 considered. The wind field vector \vec{U} is defined by *HWS*, wind direction (*WD*) and vertical wind speed (*VWS*) input variables.
 50 Each of the 6-DoF rotational and translational motions are simulated as 1 second length (DWL scan duration, from $t = 0$ s to
 51 $t = 1$ s) temporal series. They are defined as sinusoidal signals of the form

$$A \sin(360 \times f \times t - \alpha), \quad (3)$$

52 where A , f and α denote amplitude, frequency and motional phase, respectively. In a scan duration sine argument ranges from
53 $-\alpha$ to $360 \times f - \alpha$. The simulator output is the HWS measurement error, ϵ_{HWS} , defined as

$$\epsilon_{HWS} = |HWS - H\hat{W}S|, \quad (4)$$

54 where HWS is the simulated "true" wind speed used as reference and $H\hat{W}S$ is the VAD-retrieved HWS estimation.

55 In order to study the motion-induced error on the retrieved HWS, ϵ_{HWS} , a dimension reduction is needed to simplify the
56 problem. A first consideration followed in the literature [7] to alleviate the problem is to set the same motional frequency for all
57 DoF, and a wind vector with constant HWS and null VWS, therefore only allowing variable WD . Moreover, based on previous
58 expertise, we propose to approach the problem separately for rotational and translational motion.

59 *Oriented vector conventions.*- In the NED coordinate system, $WD = 0$ deg means wind blowing to the North (South-to-
60 North). v_{lidar} is defined so that the direction of v_{lidar} 0 deg for surge motion and 90 deg sway motion, for example.

61 3. RESULTS AND DISCUSSION

62 A parametric study under certain constraints is carried out in order to reduce the dimensionality of the problem to three, which
63 enables tri-dimensional plots of the absolute error on the retrieved HWS, $|\epsilon_{HWS}|$ as colorplots. Subsets selection criterion
64 was empiric with a view to foster results interpretability and large error-propagation sensitivity. Initial scan phase, θ_0 was
65 always retained as parameterization variable on account of the conical scanning principle of the VAD algorithm. Buoy motional
66 frequency was set to a typical measured value of 0.3 Hz [4]. For comparison purposes, the reference wind vector is fixed to
67 $HWS = 10$ m/s and $VWS = 0$ m/s.

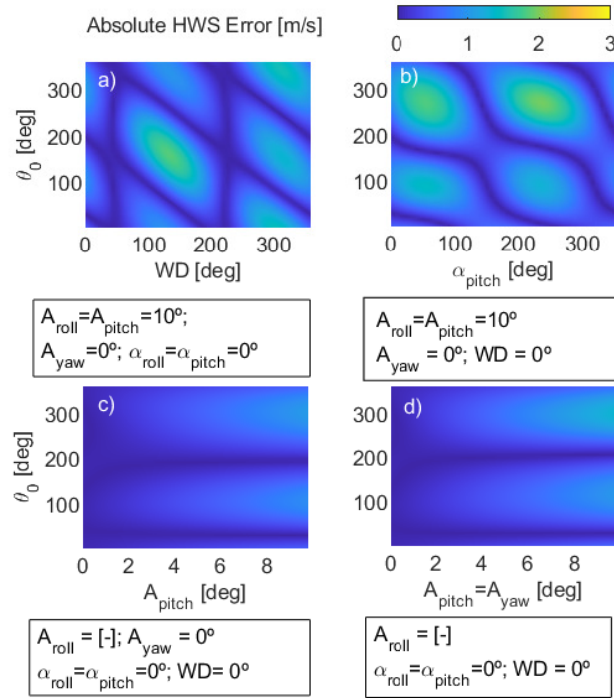


Fig. 2. ϵ_{HWS} in response to 3 DoF rotational motion (roll, pitch and yaw). Simulation parameters for each study are specified below its corresponding panel.

68 3.1. Rotational motion

69 3.1.a Wind Direction

70 *Constraints:* Roll and pitch with equal amplitude, $A = 10$ deg, and phase, $\alpha = 0$ deg. No yaw motion. Fig. 2 a.

71 Fig. 2 a shows error sensitivity in the retrieved HWS with respect to changes in WD . Results show that when the wind vector,

72 \vec{U} , is parallel to any of the rotation axes ($WD=45$ deg and 225 deg), $\epsilon_{HWS} = 0$ m/s. This is because wind-vector projections

73 onto the scanning pattern LoSs give rise to a symmetry in which there is an equal number of LoS with over/underestimated

74 radial speeds [4]. The opposite occurs when the rotation axis is perpendicular to \vec{U} ($WD = 135$ deg and $WD = 315$ deg).

75 3.1.b Roll/pitch motional phase

76 *Constraints:* $WD = 0$ and $A_{pitch} = 10$ deg (ϵ_{HWS} insensitive to roll motion, see Sect. 3.1.a). No yaw motion. Fig. 2 b.

77 Fig. 2 b studies the combined effects of buoy motional phase, varied from $\alpha_{pitch} = 0$ deg to 360 deg, on ϵ_{HWS} . Fig. 2 b shows

78 that there is not a straightforward relationship between ϵ_{HWS} , θ_0 and α_{pitch} . However, it is worth noting that when pitch shows
79 more variability (around $\alpha_{pitch}=50$ deg and 230 deg), there is higher ϵ_{HWS} . For example, for $\alpha_{pitch} \simeq 50$ deg, the pitch sine
80 argument ranges from -50 deg to 58 deg (see Equation 3) corresponding to a high slope region, and thus, high pitch variability.
81 The opposite occurs when pitch is more static ($\alpha_{pitch} = 140$ deg and 320 deg).

82 3.1.c Roll/pitch motional amplitude

83 *Constraints:* $WD=0$ (ϵ_{HWS} insensitive to roll). No yaw motion. Fig. 2 c.

84 Here we study tilt amplitude influence over ϵ_{HWS} by varying A_{pitch} from 0 deg to 10 deg. We can observe how ϵ_{HWS} grows
85 uniformly with A_{pitch} , however, at θ_0 values around 30 deg and 190 deg ϵ_{HWS} shows null values. Although this requires
86 further investigation, as we observed in Fig. 2 b, this is due to the complex relationship between θ_0 and α .

87 3.1.d Yaw motion

88 In Fig. 2 d yaw motion was added to the same simulation set-up as in panel c with A_{yaw} ranging from 0 to 10 deg. Almost
89 identical ϵ_{HWS} figures are encountered in both Fig. 2 c and d due to "almost static" yaw for these A_{yaw} values at 0.3 Hz
90 motional frequency. Yaw shows low contribution to ϵ_{HWS} .

91 3.2. Translational motion

92 3.2.a Surge and/or sway motional amplitudes

93 *Constraints:* Surge and sway equal (Fig. 3 a and unequal (Fig. 3 b amplitudes. No heave motion.

94 Fig. 3 a studies how surge and sway motions impact ϵ_{HWS} as a function of WD . Buoy translational velocity vector is defined
95 as $v_{lidar} = (v_x, v_y) = (2, 2)$ with $|v_{lidar}| = \sqrt{8}$ and orientation 45 deg being v_x surge and v_y sway with $A = 2$ m/s and $\alpha = 0$
96 deg. Results show that when the wind vector \vec{U} is parallel to v_{lidar} ($WD=45$ deg and 225 deg), high ϵ_{HWS} can be found. This
97 is due to the fact that the lidar-measured radial velocities are the addition of v_{lidar} and \vec{U} . Thus, negligible ϵ_{HWS} can be found
98 at v_{lidar} perpendicular to \vec{U} ($WD=135$ and 315 deg). This is corroborated in Fig. 3 b where there is $v_{lidar} = (\sqrt{8}, 0)$ (same

99 module, N direction). Now the highest ϵ_{HWS} are obtained around WD of 0 deg and 180 deg, and the lowest around WD of
 100 90 deg and 270 deg.

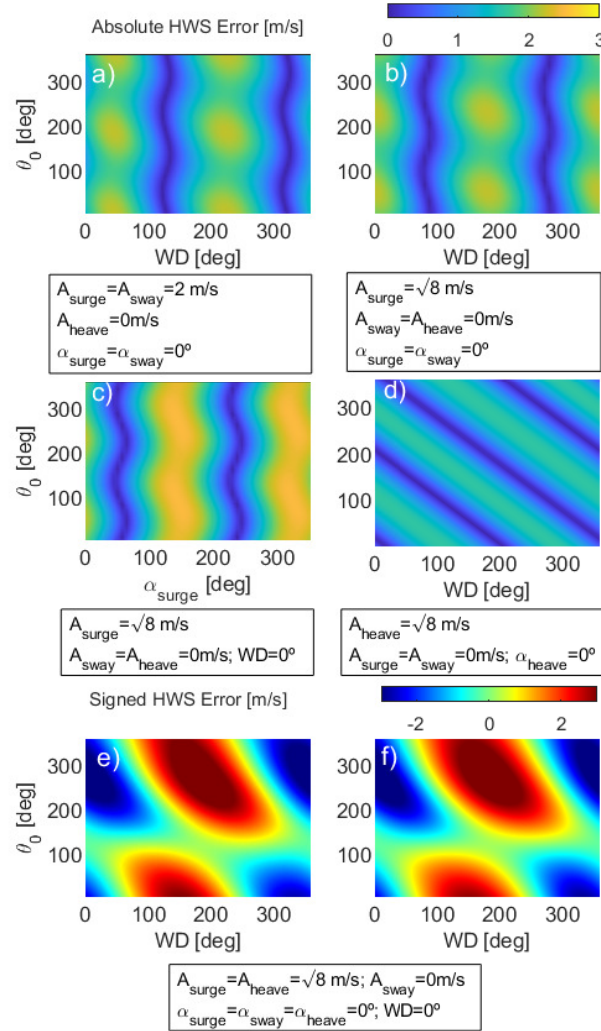


Fig. 3. ϵ_{HWS} in response to 3 DoF translational motion (surge, sway and heave). Simulation parameters for each study are specified below its corresponding panel.

100

101 3.2.b Surge/sway motional phase

102 *Constraints:* $WD=0$ and $A_{surge} = \sqrt{8}$ m/s (ϵ_{HWS} insensitive to sway motion). No heave motion. Fig. 3 c.

103 Fig. 3 c studies the influence of horizontal motion phase, varied from $\alpha_{surge} = 0$ deg to 360 deg, on ϵ_{HWS} . Low ϵ_{HWS}

104 figures are noticed when surge is close to 0 m/s ($\alpha_{surge} = 57$ deg and 235 deg). For example, for $\alpha_{surge} = 57$ deg the sine

105 argument ranges from -57 to 51 deg corresponding to surge values close to 0 m/s. The opposite is encountered around surge

106 peaks ($\alpha_{surge} = 150$ deg and 320 deg).

107 **3.2.c Heave**

108 *Constraints:* Heave only with $A_{heave} = \sqrt{8}$ m/s and $\alpha_{heave} = 0$ deg. Fig. 3 d.

109 In Fig. 3 d heave impact on ϵ_{HWS} as a function of WD is studied. Fig. 3 d shows a lower ϵ_{HWS} figure compared to a, b and c
110 panels. In contrast to previous discussion cases (Fig. 3 a-c), Fig. 3 d shows a periodic error pattern in which diagonally oriented
111 signatures evidence that the effects of variables scan phase, θ_0 , and WD on the retrieved HWS error, ϵ_{HWS} , follow a linear
112 relationship, i.e., HWS error can be expressed as $\epsilon_{HWS} = C \sin(u)$, where $u = \theta_0 + WD$.

113 **3.2.d Combined surge, sway and heave**

114 *Constraints:* Surge and heave with equal motional amplitudes $A = \sqrt{8}$ and $WD = 0$ deg. No sway motion. Fig. 3 e, f.

115 According to the surge/sway symmetry properties in relation to WD enunciated in Sect. 3.2.a, the study next is representative
116 of 3 DoF motion (surge, sway and heave).

117 Fig. 3 e shows 3 DoF motion effect over ϵ_{HWS} as a function of WD . In contrast to Fig. 3 a-d, Fig. 3 e plots ϵ_{HWS} as
118 a signed quantity and evidences a complex periodic pattern diagonally oriented. This same Fig. 3 e is found in Fig. 3 f when
119 Fig. 3 b and Fig. 3 d are added up retaining ϵ_{HWS} as a signed quantity on account of the superposition principle.

120

4. CONCLUSIONS

121 A FDWL motion simulator has been presented for the case of rotational and translational motion (6 DoF, 3 s motional period).

122 The system simulates the 50 LoS measurements in a conical scan and the wind vector retrieval by the VAD algorithm under
123 motion influence. The simulator was used to study the impact of different motional parameters over HWS retrieval error ϵ_{HWS} .

124 Simulation results showed that in the presence of motion, ϵ_{HWS} has a strong dependency on initial scan phase θ_0 . Moreover,
125 the directions of rotation axis and translational velocity vector (with respect to WD) showed great impact on ϵ_{HWS} (averaged
126 out in 10 min basis). 3 DoF superposition principle was corroborated for translational motion.

127 The simulator presents itself as a useful tool for understanding particular lidar motion scenarios contribution to HWS
128 measurements. However, further analysis of the lidar initial scan phase is needed. Additionally, the introduction of non-
129 homogeneous wind fields would give insights in how floating lidars are able to retrieve the wind vector in turbulent wind
130 scenarios.

131 5. References

- 132 [1] Carbon Trust, “Carbon trust offshore wind accelerator roadmap for the commercial acceptance of floating LIDAR technol-
133 ogy,” Carbon Trust, Tech. Rep., Nov. 2013.
- 134 [2] O. Bischoff, I. Würth, P. Cheng, J. Tiana-Alsina, and M. Gutiérrez, “Motion effects on lidar wind measurement data of the
135 EOLOS buoy,” in *Proc. 1st Int. Conf. Renew. Ener. Off.*, *RENEW 2014*, RENEW 2014, Ed., Nov. 2014.
- 136 [3] F. Kelberlau, V. Neshaug, L. Lønseth, T. Bracchi, and J. Mann, “Taking the Motion out of Floating Lidar: Turbulence
137 Intensity Estimates with a Continuous-Wave Wind Lidar,” *Remote Sens.*, vol. 12, no. 898, 2020.
- 138 [4] J. Tiana-Alsina, M. A. Gutiérrez, I. Würth, J. Puigdefàbregas, and F. Rocadenbosch, “Motion compensation study for a
139 floating doppler wind lidar,” in *2015 IEEE Int. Geosci. Remote. Se. (IGARSS)*, July 2015.
- 140 [5] M. Gutiérrez-Antuñano, J. Tiana-Alsina, A. Salcedo, and F. Rocadenbosch, “Estimation of the Motion-Induced Horizontal-
141 Wind-Speed Standard Deviation in an Offshore Doppler Lidar,” *Remote Sens.*, vol. 10, no. 12, p. 2037, dec 2018.
- 142 [6] M. Pitter, C. Slinger, and M. Harris, “Introduction to continuous-wave Doppler lidar,” *Remote Sensing for Wind Energy*.
- 143 [7] M. A. Gutierrez-Antunano, J. Tiana-Alsina, F. Rocadenbosch, J. Sospedra, R. Aghabi, and D. Gonzalez-Marco, “A wind-
144 lidar buoy for offshore wind measurements: First commissioning test-phase results,” in *IEEE Int. Geosci. Remote. Se.*
145 *(IGARSS)*. IEEE, Jul. 2017.